Computers & Geosciences 107 (2017) 37–48

Contents lists available at ScienceDirect

Computers & Geosciences

journal homepage: www.elsevier.com/locate/cageo

Research paper

# Methods to enhance seismic faults and construct fault surfaces

Xinming Wu[a,*], Zhihui Zhu[b]

[a] Bureau of Economic Geology, University of Texas at Austin, Austin, TX, USA
[b] Department of Electrical Engineering and Computer Science; Colorado School of Mines, Golden, CO, USA

## ABSTRACT

Faults are often apparent as reflector discontinuities in a seismic volume. Numerous types of fault attributes have been proposed to highlight fault positions from a seismic volume by measuring reflection discontinuities. These attribute volumes, however, can be sensitive to noise and stratigraphic features that are also apparent as discontinuities in a seismic volume. We propose a matched filtering method to enhance a precomputed fault attribute volume, and simultaneously estimate fault strikes and dips. In this method, a set of efficient 2D exponential filters, oriented by all possible combinations of strike and dip angles, are applied to the input attribute volume to find the maximum filtering responses at all samples in the volume. These maximum filtering responses are recorded to obtain the enhanced fault attribute volume while the corresponding strike and dip angles, that yield the maximum filtering responses, are recoded to obtain volumes of fault strikes and dips. By doing this, we assume that a fault surface is locally planar, and a 2D smoothing filter will yield a maximum response if the smoothing plane coincides with a local fault plane. With the enhanced fault attribute volume and the estimated fault strike and dip volumes, we then compute oriented fault samples on the ridges of the enhanced fault attribute volume, and each sample is oriented by the estimated fault strike and dip. Fault surfaces can be constructed by directly linking the oriented fault samples with consistent fault strikes and dips. For complicated cases with missing fault samples and noisy samples, we further propose to use a perceptual grouping method to infer fault surfaces that reasonably fit the positions and orientations of the fault samples. We apply these methods to 3D synthetic and real examples and successfully extract multiple intersecting fault surfaces and complete fault surfaces without holes.

## 1. Introduction

Faults are one type of geologically structural surfaces that can be extracted from a seismic volume. To extract fault surfaces from a seismic image, we often need to first distinguish faults from the other structures that are also present in the volume. Therefore, to extract fault surfaces, we often first compute a fault attribute volume, in which only the faults are most prominent.

Faults are often recognized as low continuity, or equivalently, high discontinuity in seismic reflectors (Hale, 2013). Therefore, to automatically detect faults, some methods compute fault attributes that measure reflection continuity such as semblance (Marfurt et al., 1998) and coherency (Marfurt et al., 1999; Bakker, 2002; Wu, 2017), or those measure reflection discontinuity such as variance (Van Bemmel and Pepper, 2000; Randen et al., 2001) and gradient magnitude (Aqrawi and Boe, 2011).

However, reflector discontinuity alone might not be sufficient to detect faults, because incoherent noise and stratigraphic features can also cause reflector discontinuities in a seismic volume. Moreover, faults may not be apparent as reflector discontinuities in cases where fault displacements are approximately equal to the dominant period (or wavelength) of those reflectors. In these cases, reflector discontinuities corresponding to faults can be widely separated or interrupted (Hale, 2013).

Therefore, Gersztenkorn and Marfurt (1999) suggest to measure continuity or discontinuity using a larger vertical window for fault detection while using a larger horizontal window for detecting stratigraphic features. By using a window with vertically larger size, fault

* Corresponding author.
*E-mail addresses:* xinwucwp@gmail.com (X. Wu), zzhu@mines.edu (Z. Zhu).

http://dx.doi.org/10.1016/j.cageo.2017.06.015
Received 6 February 2017; Received in revised form 24 May 2017; Accepted 19 June 2017
Available online 20 June 2017
0098-3004/ Published by Elsevier Ltd.

features can be enhanced and stratigraphic features can be suppressed because faults are often more vertically aligned in a seismic volume than the stratigraphic features. However, faults are seldom vertical. A better way to enhance the discontinuities corresponding to faults is to measure reflector discontinuities in planes aligned with the strikes and dips of the faults (Neff et al., 2000; Cohen et al., 2006). However, the computational cost of these methods can be high because the fault strikes and dips are often unknown. For each sample, they need to measure reflector discontinuities over all possible combinations of fault strikes and dips to find the largest discontinuity. Hale (2013) proposes an efficient implementation of such a scanning processing to compute a fault-oriented semblance or fault likelihood volume to highlight fault positions from a seismic volume.

Constructing fault surfaces from fault attribute volumes often requires additional processing. Pedersen et al., (2002, 2003) propose to use the ant tracking method to merge small fault segments together to form larger fault surfaces. Similarly, some other methods (Gibson et al., 2005; Admasu et al., 2006; Kadlec et al., 2008) also try to grow larger fault surfaces from smaller patches. Hale (2013) uses a method, similar to the one developed by Schultz et al. (2010), to construct fault surfaces that coincide with ridges of a fault likelihood volume. Hough transform is an alternative way to construct fault surfaces from seismic fault attributes (Wang and AlRegib, 2014; Wang and AlRegib et al., 2014). Wu and Hale (2016) compute fault surfaces by linking oriented fault samples constructed from attributes of fault likelihoods, strikes, and dips.

In more general context, numerous methods have been proposed to construct surfaces from a given set of oriented or unoriented points (Guy and Medioni, 1993; Tang, 2000; Kazhdan et al., 2006; Lipman et al., 2007; Kazhdan and Hoppe, 2013; Berger et al., 2014; Wu, 2016).

Some of these methods are limited to extract closed and single surfaces, and therefore are not applicable to construct fault surfaces. However, the tensor-voting method (Guy and Medioni, 1993; Tang, 2000) has been used in computer graphics to construct multiple open surfaces and intersecting surfaces. Giving oriented fault samples estimated at fault positions, this method can effectively construct fault surfaces which may intersect with each other.

In this paper, we apply a matched filtering algorithm to enhance a precomputed fault attribute volume while at the same time estimating fault strikes and dips. Using the enhanced fault attribute volume together with the estimated fault strike and dip volumes, we then construct fault samples on the ridges of the enhanced fault attribute volume. Each fault sample corresponds to one and only one seismic sample, and is oriented by the corresponding fault strike and dip. Fault surfaces can be constructed by directly linking nearby fault samples with consistent strikes and dips in cases where fault geometry is simple (no intersecting faults) and fault samples are consistently aligned. In more complicated cases with noisy fault samples and missing samples, we propose to use a *tensor-voting* method (Guy and Medioni, 1993; Tang, 2000; Moreno et al., 2011) to construct fault surfaces that reasonably fit locations and orientations of fault samples and fill holes due to the missing samples.

## 2. Fault enhancement and fault orientations

Fault surfaces are often extracted from a fault attribute volume that measures reflection discontinuity and therefore highlights fault positions. A fault attribute volume is often sensitive to noise and stratigraphic features that also produce reflection discontinuities in a seismic volume. Therefore, a helpful step before fault extraction is to smooth the fault attribute volume along fault orientations so that features unrelated to faults are suppressed and fault features are enhanced. Fault orientations such as strikes and dips are also helpful to construct fault surfaces. We will discuss how to simultaneously enhance fault features in a fault attribute volume and estimate fault strikes and dips by using a matched filtering method.

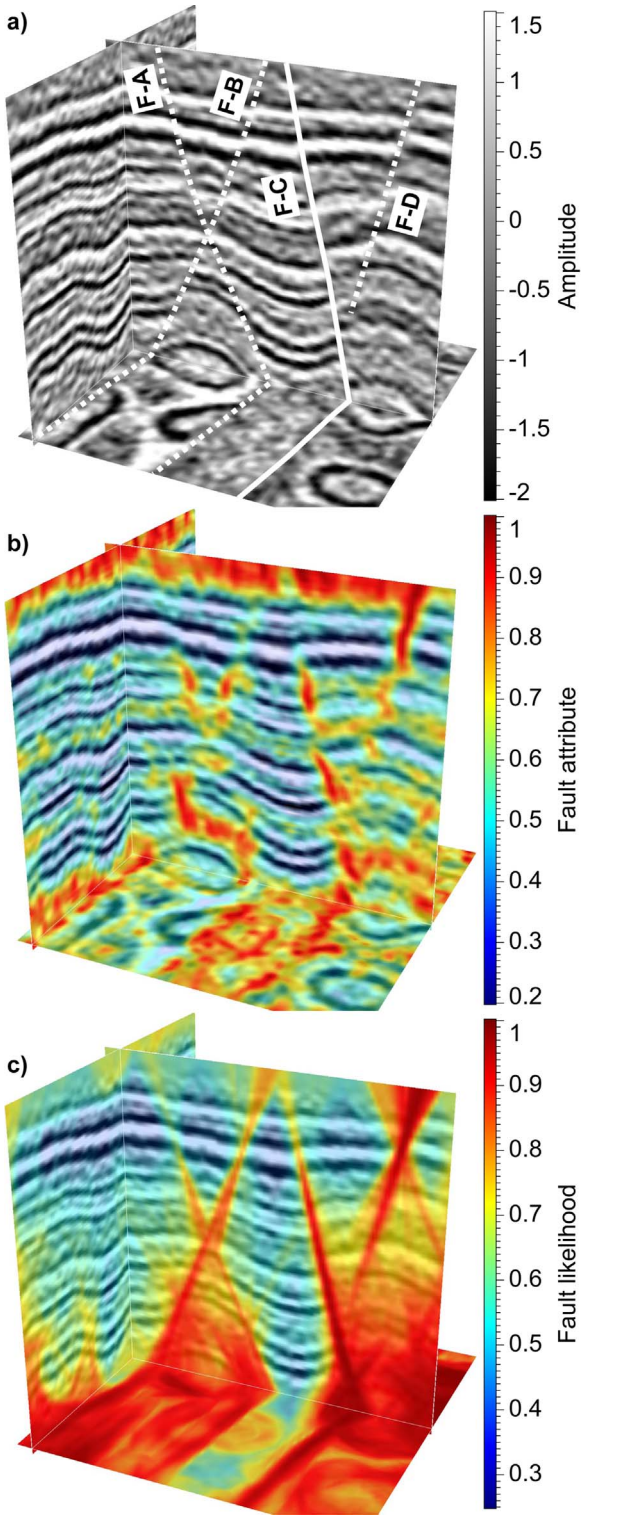


**Fig. 1.** A 3D seismic volume (a) is displayed with a fault attribute volume (b) (1-semblance), and a fault likelihood volume (c).

### 2.1. Fault attributes

We created a 3D synthetic seismic volume (Fig. 1(a)) with different types of faults to demonstrate our methods for enhancing fault attributes and constructing fault surfaces. As denoted by the white lines in Fig. 1(a), this synthetic volume contains two intersecting faults F-A and F-B, a reverse fault F-C, and a smaller normal fault F-D.

To automatically highlight fault positions from the seismic volume, we compute a fault attribute volume (Fig. 1(b)) from a structure-oriented semblance volume (Hale, 2009):

$$p = \frac{\langle g \rangle_s^2}{\langle g^2 \rangle_s}, \tag{1}$$

where $g$ is a seismic volume like the one in Fig. 1(a). $\langle \cdot \rangle_s$ denotes structure-oriented smoothing of whatever is inside the angle brackets. By applying this smoothing $\langle \cdot \rangle_s$ to both the numerator ($g$) and denominator ($g^2$) in Eq. (2), the semblance measures reflection continuity within the planes that align with seismic reflection.

As semblance is a measure of reflection continuity, we compute the fault attribute volume (Fig. 1(b)) by $1 - p$ to highlight faults which are indicated by reflection discontinuity. In this volume (Fig. 1(b)), some features with relatively high values (denoted by red) indicate positions of the faults. However, the fault features in the attribute volumes are inconsistent and interrupted, as in Fig. 1(b). In addition, incoherent noise unrelated to faults is also highlighted in this attribute volume (Fig. 1(b)).

To suppress features corresponding to noise and enhance fault features, Hale (2013) proposes to compute a fault-oriented semblance:

$$p = \frac{\langle \langle g \rangle_s^2 \rangle_f}{\langle \langle g^2 \rangle_s \rangle_f}, \tag{2}$$

where $\langle \cdot \rangle_f$ denotes an additional smoothing in fault strike and dip directions. This smoothing $\langle \cdot \rangle_f$ can improve the stability of the semblance computation because the semblance ratios can vary wildly where the numerators and denominators are small. This smoothing $\langle \cdot \rangle_f$ can also link together fault features which might be interrupted or widely separated as shown in Fig. 1(b).

A fault likelihood volume, like the one in Fig. 1(c), is then computed from the fault-oriented semblance by $1 - p^8$. We observe that the fault features in this fault likelihood volume are much more consistent and continuous than those in Fig. 1(b) which is computed from a conversional semblance volume.

One problem for computing such a fault-oriented semblance is that the fault locations and orientations are unknown. To solve this problem, Hale (2013) smoothes the semblance numerator and denominator over a range of possible combinations of strike and dip to find the one orientation that maximizes the fault likelihood (or minimizes the semblance) for each sample. This maximum value for each sample is recorded in the fault likelihood volume as shown in Fig. 1(c). The strike and dip angles that yield the maximum likelihood are recorded as an estimation of the fault orientations. Neff et al. (2000) and Cohen et al. (2006) also perform a similar scanning processing to compute fault attributes.

One advantage of these methods is that they compute better fault attribute volumes with more consistent fault features, like those in Fig. 1(c), compared to those in Fig. 1(b). Another advantage is that they can provide an estimation of fault orientations at the same time as computing a fault attribute volume. However, the computational cost of these methods can be high because of the scanning over a lot of orientations for each sample. Hale (2013) reduces the computational cost by implementing this fault-oriented smoothing with recursive smoothing filters whose costs are independent on the extent of smoothing.

### 2.2. Matched filtering to enhance faults and estimate fault orientations

To enhance a fault attribute volume like the one in Fig. 1(b), we expect to smooth the volume along fault orientations, so that the fault features in the enhanced volume are more continuous and prominent, as shown in Fig. 2(a). To smooth along fault orientations, a traditional structure-oriented smoothing method requires first estimating the fault orientations. However, general orientation estimation techniques such as structure-tensor methods (Van Vliet and Verbeek, 1995; Fehmers and Höcker, 2003) and the plane-wave destruction method (Fomel, 2002) have difficulties in estimating fault orientations from a fault attribute volume (Fig. 1(b)) because the attribute features are discontinuous and most attribute values are nearly zero. The method described by Marfurt (2006) might be better to estimate the fault orientations by scanning over all possible orientations for each point to find the one orientation that produces the maximum coherency. However, this scanning method can be computationally expensive to estimate orientations of these discontinuous fault features (Fig. 1(b)), which often requires large scanning windows.

Here we use an efficient matched filtering method, similar to the one described by Hale (2013), to simultaneously estimate fault strikes and dips, and obtain an enhanced fault attribute volume from an input fault attribute volume (Fig. 1(b)). In this method, we smooth the input volume $f(\mathbf{x})$ in different planes defined by all possible combinations of fault strike and dip angles, and record the maximum smoothing values and the corresponding strike and dip angles in the three volumes of enhanced fault attribute, fault strikes and fault dips. By doing this, we assume that a fault surface is locally planar and the 2D smoothing filter (oriented by a combination of strike and dip angles) will yield the maximum smoothing response if the smoothing plane coincides with a local fault plane. For each sample $\mathbf{x}$, we accumulate all smoothed values (in different directions) in a volume $c(\mathbf{x})$:

$$c(\mathbf{x}) = \sum_{\phi_k \in \phi_S} \sum_{\theta_k \in \theta_S} \langle f(\mathbf{x}) \rangle_{\phi_k, \theta_k}, \tag{3}$$

where $\phi_S = \{0°, d_\phi, 2d_\phi, \ldots, 360°\}$, and $\theta_S = \{\theta_{\min}, \theta_{\min} + d_\theta, \theta_{\min} + 2d_\theta, \ldots, \theta_{\max}\}$. $d_\phi$ and $d_\theta$ are user defined parameters and often are bigger than one. $\theta_{\min}$ and $\theta_{\max}$ define the range of the fault dip angles apparent in a 3D seismic volume. $\langle f(\mathbf{x}) \rangle_{\phi_k, \theta_k}$ represents smoothing the volume $f(\mathbf{x})$ along a plane defined by the strike ($\phi_k$) and dip ($\theta_k$) angles.

We also record the maximum smoothed value in a volume $m(\mathbf{x}) = \max(\langle f(\mathbf{x}) \rangle_{\phi_k, \theta_k}: \phi_k \in \phi_S, \theta_k \in \theta_S)$ and record the corresponding strike and dip that generate this maximum value in volumes $\phi(\mathbf{x})$ and $\theta(\mathbf{x})$, respectively. These volumes $\phi(\mathbf{x})$ and $\theta(\mathbf{x})$ represent estimations of fault strikes and dips, because the fault attribute features are most consistent in directions defined by these strikes and dips. An enhanced fault attribute volume $h(\mathbf{x})$ can be computed by

$$h(\mathbf{x}) = \frac{m(\mathbf{x}) - \bar{c}(\mathbf{x})}{m(\mathbf{x})}, \tag{4}$$

where $\bar{c}(\mathbf{x}) = \frac{c(\mathbf{x})}{N}$, and $N$ represents the number of combinations of strikes and dips that are scanned in the matched filtering method.

In this method, most of the computational time is spent on the smoothing ($\langle f(\mathbf{x}) \rangle_{\phi_k, \theta_k}$) along planes oriented by all possible combinations of the fault strike ($\phi_k$) and dip ($\theta_k$) angles. We use the strategy discussed by Hale (2013) to perform this oriented smoothing efficiently. In this strategy, for each fault strike angle $\phi_k$, we rotate the

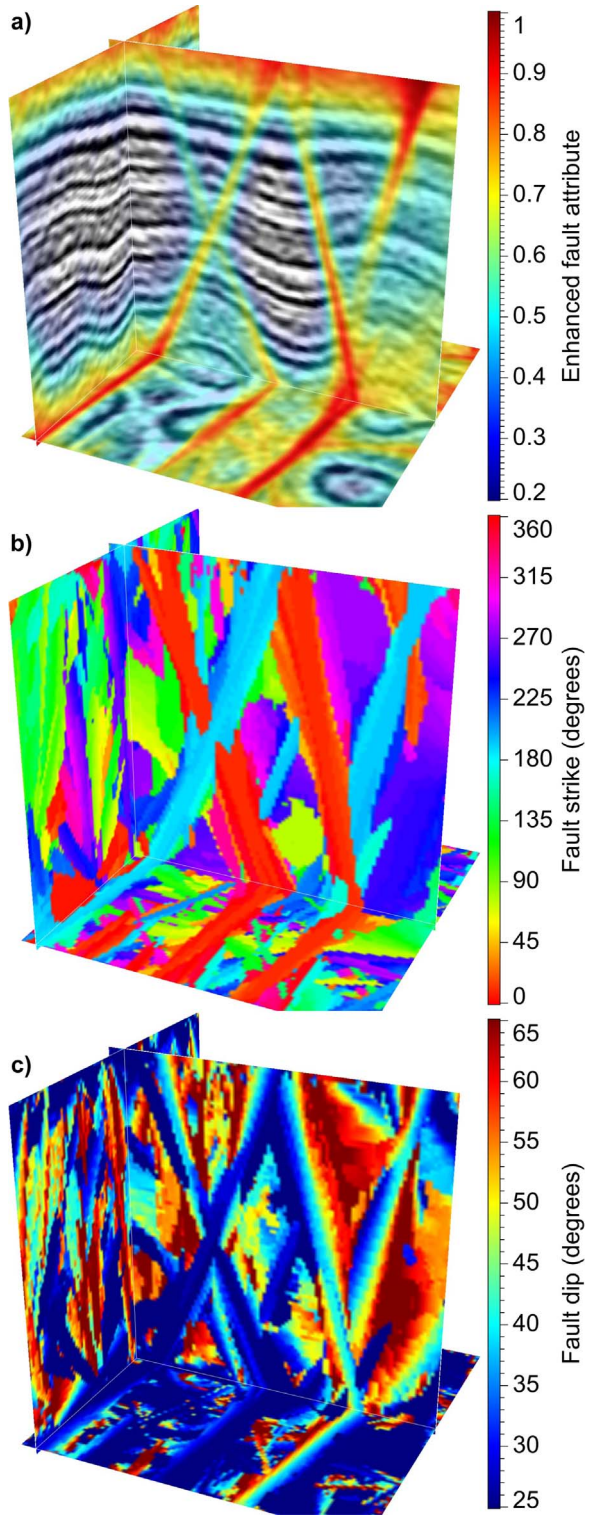


**Fig. 2.** The matched filtering method is applied to the fault attribute volume (Fig. 1(b)) to simultaneously compute an enhanced fault attribute volume (a), a fault strike volume (b), and a fault dip volume (c).

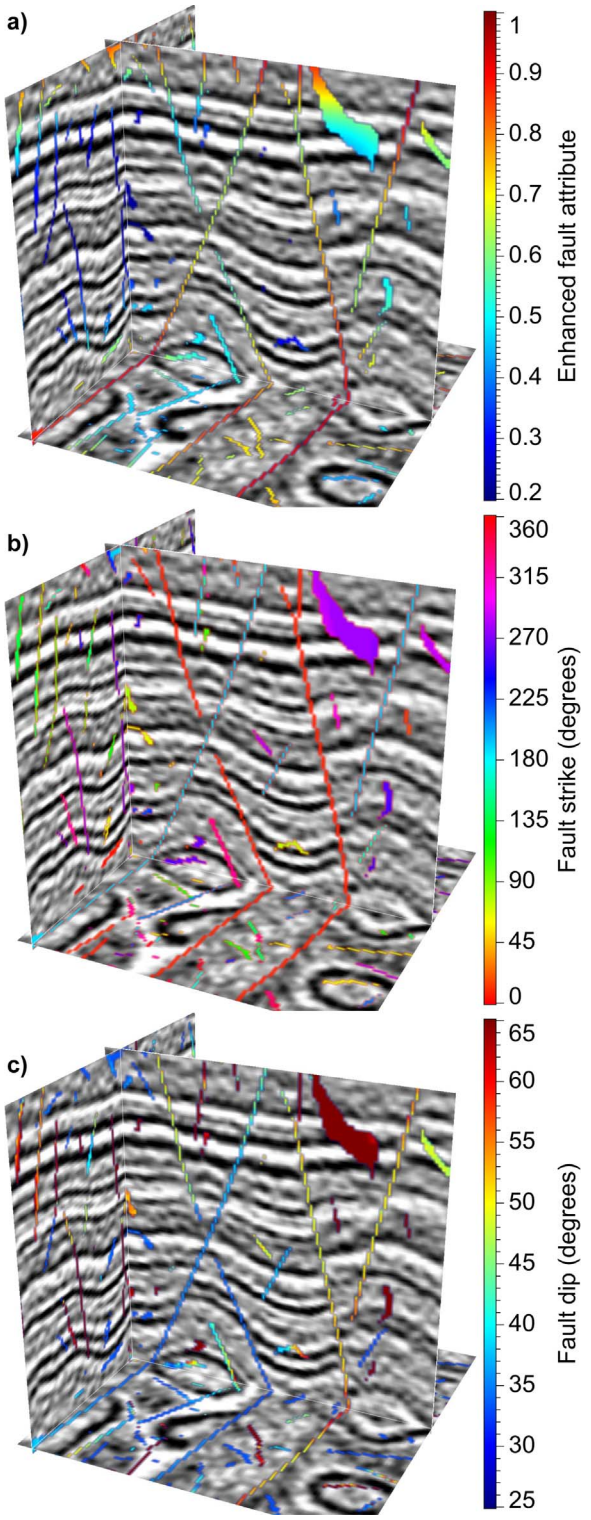


**Fig. 3.** Three thinned volumes of enhanced fault attribute (a), strike (b), and dip (c) volumes are obtained by keeping only the values on the ridges of the enhanced fault attribute volume (Fig. 2(a)).

volume $f(\mathbf{x})$ to align the fault strike direction with the crossline axis. We then apply a highly efficient recursive two-side-exponential filter to smooth the rotated volume horizontally in the crossline direction before scanning over fault dips $\theta_k \in \theta_S$. In scanning over fault dips, for each dip angle $\theta_k$, we shear the rotated and smoothed volume horizontally to make faults with that dip appear to be vertical. We then

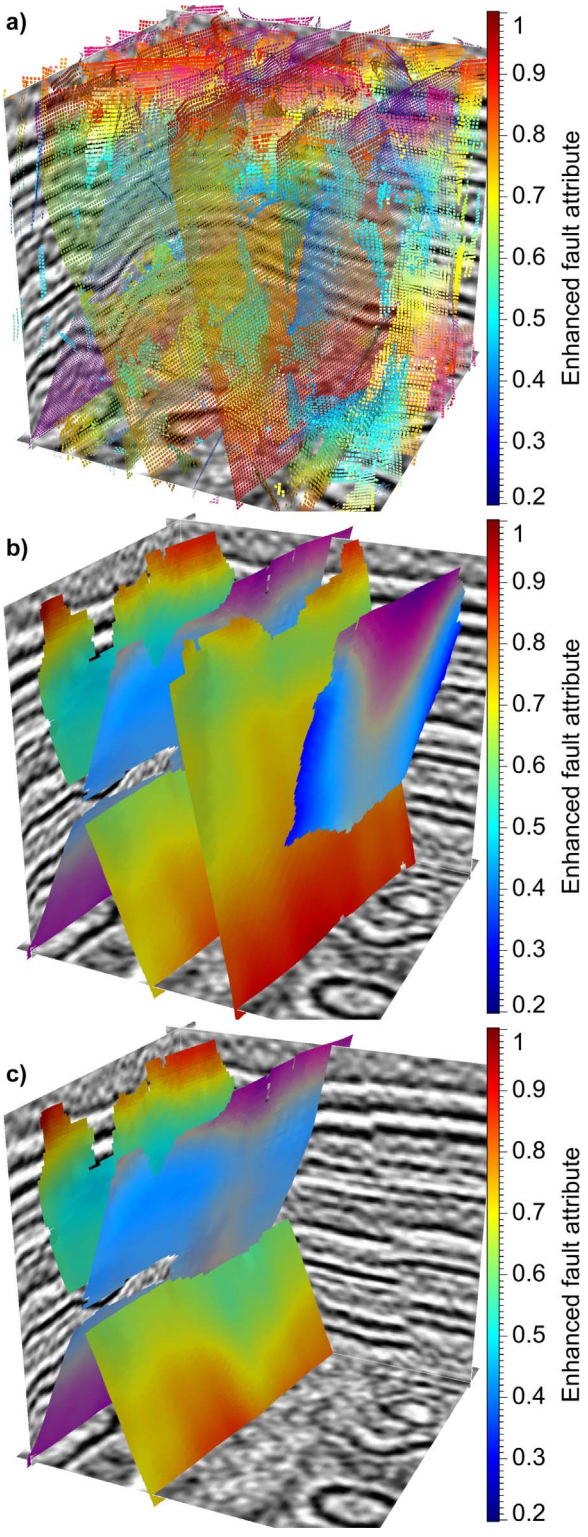


**Fig. 4.** The three thinned fault volumes (Fig. 3) are represented, all at once, as fault samples which are displayed as small squares (a). Each square in (a) is colored by the enhance fault attribute and oriented by fault strike and dip. Those consistent fault samples in (a) are linked to construct fault surfaces in (b). Gaps or holes are apparent on the two intersecting faults (c), especially at the intersection.

apply the recursive exponential filter to smooth the sheared volume vertically, and unshear the smoothed volume.

More details of the algorithm are described in the following pseudo codes:

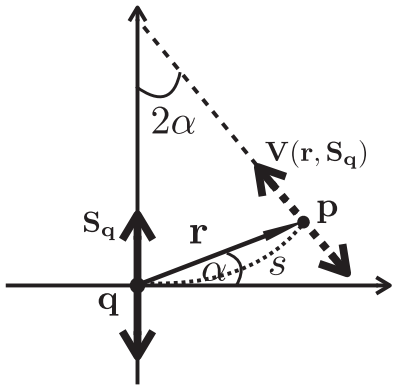


**Fig. 5.** A stick tensor $\mathbf{S_q}$ at the voter $\mathbf{q}$ propagates a voting tensor $\mathbf{V}(\mathbf{r}, \mathbf{S_q})$ to the receiver $\mathbf{p}$.

**Algorithm 1.** Matched filtering for fault enhancing and fault orientation estimation.

**input:** $f(\mathbf{x})$
**initial output:** $h(\mathbf{x}) = 0,\ \phi(\mathbf{x}) = 0,\ \theta(\mathbf{x}) = 0$
initialize $c(\mathbf{x}) = 0,\ m(\mathbf{x}) = 0$
**for** $\phi_k$:=0° **to** 360° **step** $d_\phi$ **do**
  $r(\mathbf{x})$= **rotate** $f(\mathbf{x})$ **to align strike** $\phi_k$ with crossline
  $r(\mathbf{x})$= smooth $r(\mathbf{x})$ horizontally in crossline
  initialize $m_t(\mathbf{x}) = 0$, $\theta_t(\mathbf{x}) = 0$, $c_t(\mathbf{x}) = 0$
  **for** $\theta_k$:=$\theta_{\min}$ **to** $\theta_{\max}$ **step** $d_\theta$ **do**
    $s(\mathbf{x})$= shear $r(\mathbf{x})$ to align dip $\theta_k$ vertically
    $s(\mathbf{x})$= smooth $s(\mathbf{x})$ vertically
    $s(\mathbf{x})$= unshear $s(\mathbf{x})$
    **if** $s(\mathbf{x}_i) > m_t(\mathbf{x}_i)$ **then**
      $\theta_t(\mathbf{x}_i) = \theta_k$
      $m_t(\mathbf{x}_i) = s(\mathbf{x}_i)$
      $c_t(\mathbf{x}_i) = c_t(\mathbf{x}_i) + s(\mathbf{x}_i)$
    **end if**
  **end for**
  $\theta_t(\mathbf{x})$= unrotate $\theta_t(\mathbf{x})$ by $\phi_k$
  $m_t(\mathbf{x})$= unrotate $m_t(\mathbf{x})$ by $\phi_k$
  $c_t(\mathbf{x})$= unrotate $c_t(\mathbf{x})$ by $\phi_k$ **then**
  **if** $m_t(\mathbf{x}_i) > m(\mathbf{x}_i)$
    $\phi(\mathbf{x}_i) = \phi_k$
    $\theta(\mathbf{x}_i) = \theta_t(\mathbf{x}_i)$
    $m(\mathbf{x}_i) = m_t(\mathbf{x}_i)$
    $c(\mathbf{x}_i) = c(\mathbf{x}_i) + c_t(\mathbf{x}_i)$
  **end if**
**end for**
$n_\phi = \frac{360}{d_\phi},\ n_\theta = \frac{\theta_{\max} - \theta_{\min}}{d_\theta},\ \bar{c}(\mathbf{x}) = \frac{c(\mathbf{x})}{n_\phi * n_\theta}$
**output:** $\phi(\mathbf{x})$, $\theta(\mathbf{x})$, **and** $h(\mathbf{x}) = \frac{m(\mathbf{x}) - \bar{c}(\mathbf{x})}{m(\mathbf{x})}$

To demonstrate the effectiveness of the proposed method, we use the precomputed fault attribute volume (Fig. 1(b)) as the input and obtain the enhanced fault attribute volume (Fig. 2(a)), strike volume (Fig. 2(b)), and dip volume (Fig. 2(c)). The fault features in the enhanced fault volume (Fig. 2(a)) are much more consistent and continuous than those in the original fault attribute volume (Fig. 1(b)). Compared to the fault likelihood volume (Fig. 1(c)), the enhanced fault attribute volume (Fig. 2(a)) displays similar but cleaner fault features. More importantly, this matched filtering method is not limited to compute a fault likelihood (fault-oriented semblance) volume (Hale, 2013), instead, it is applicable to enhance any type of fault attributes or multiple types of attributes. In addition, the cost of computing such an enhanced fault volume (Fig. 2(a)) is only half of computing a fault likelihood volume (Fig. 1(c)).

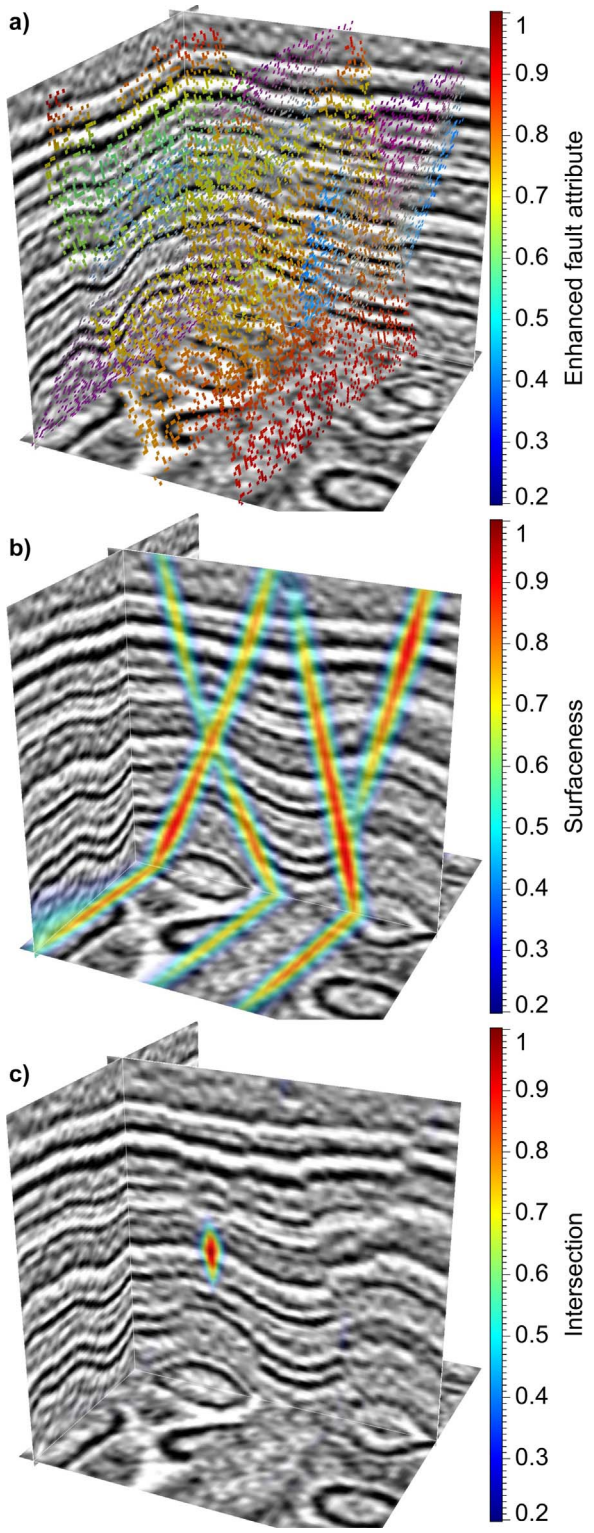


**Fig. 6.** Twenty five percent of fault samples (a) are randomly chosen from fault surfaces in Fig. 4(b). These fault samples (a) are used to compute another volumes of surfaceness (b) and fault intersection (c), which indicate the positions of faults and fault intersections, respectively.

### 2.3. Fault samples and surfaces

In the enhanced fault attribute volume (Fig. 2(a)), high values (denoted by red) indicate fault positions. However, faults are generally not apparent as thick as the features displayed in this enhanced fault attribute volume (Fig. 2(a)). Therefore, we keep only the attribute values on the ridges of the fault volume, and we set values elsewhere to be zero to obtain the thinned fault volume shown in Fig. 3(a). We also compute the corresponding thinned fault strike (Fig. 3(b)) and dip (Fig. 3(b)) volumes by keeping only the strike and dip angles on the ridges of the enhanced fault volume (Fig. 2(b))

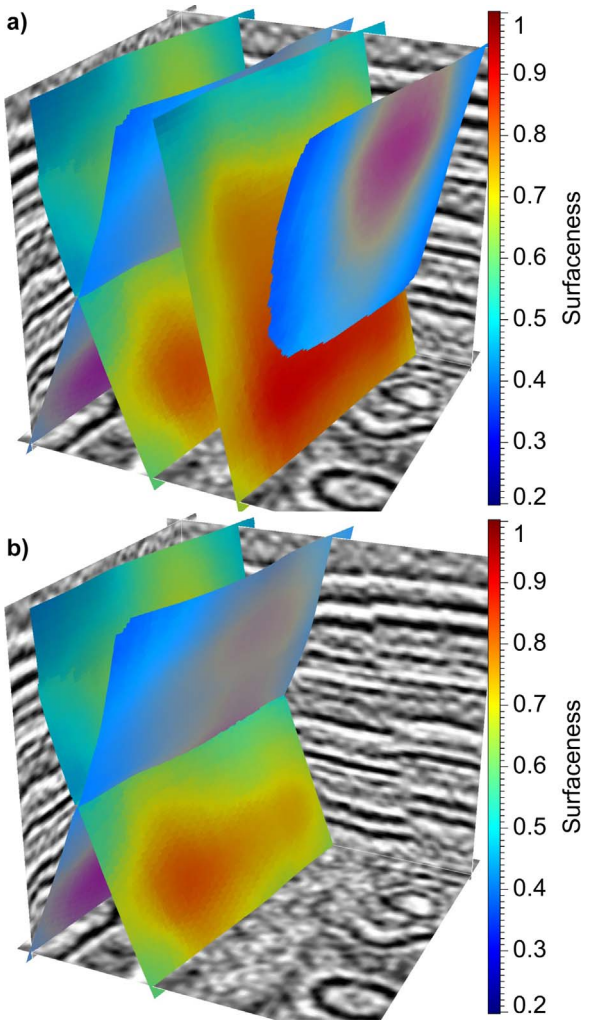


**Fig. 7.** Complete fault surfaces (a) without holes are extracted from the fault surfaceness volume (Fig. 4b). The fault intersection attribute (Fig. 4c) is also helpful to construct intersecting fault surfaces (b) by indicating the intersection locations.

Because most samples in the three thinned fault volumes (Figs. 3(a), (b), and (c)) are zero, we can display these volumes, all at once, as fault samples (Fig. 4(a)) as discussed by Wu and Hale (2016). As shown in Fig. 4(a), each fault sample is represented as a colored and oriented square. The color of each square denotes the enhanced fault attribute value, and the orientation of each square represents the fault strike and dip. As discussed by Wu and Hale (2016), fault surfaces can be constructed from these fault samples by simply linking nearby fault samples with consistent fault strikes and dips. As shown in Fig. 4(a), most fault samples are aligned approximately coplanar and are linked to form fault surfaces as shown in Fig. 4(b). Some misaligned fault samples (often with low fault likelihoods) are also apparent in Fig. 4(a), however, cannot be linked together to form locally planar fault surfaces of significant size. We filter out surfaces with small sizes, and keep only those with significant numbers of fault samples. For example, in Fig. 4(b), we have discarded small fault surfaces and kept only the five largest surfaces.

There are only four faults created in the synthetic seismic volume shown in Fig. 1(a). We obtain five faults here because the fault A is separated into two independent fault patches by a gap apparent at the

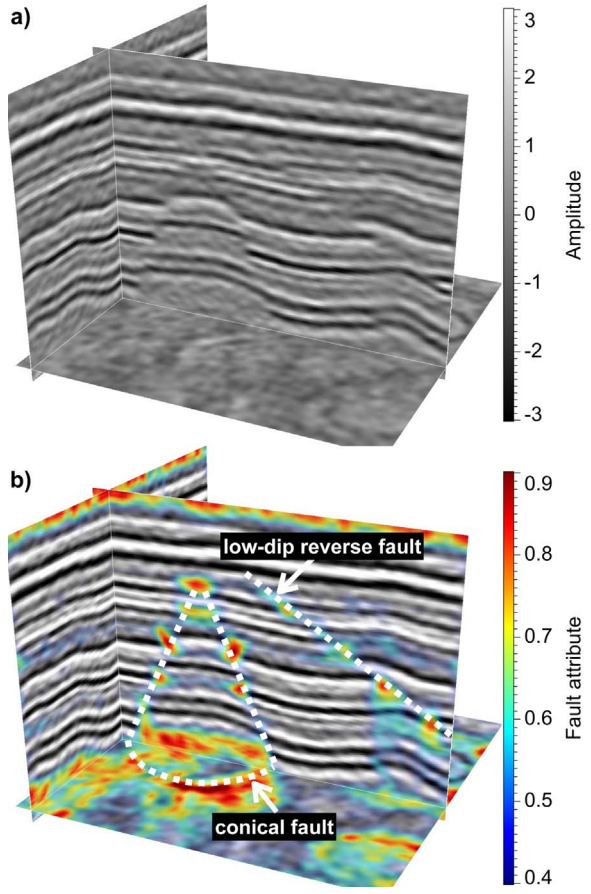


**Fig. 8.** A 3D seismic volume (a) is displayed with a fault attribute volume (b) (1-semblance), which highlights some positions of the faults but the fault feature in this attribute volume are discontinuous and therefore cannot be directly used to extract the corresponding fault surfaces.

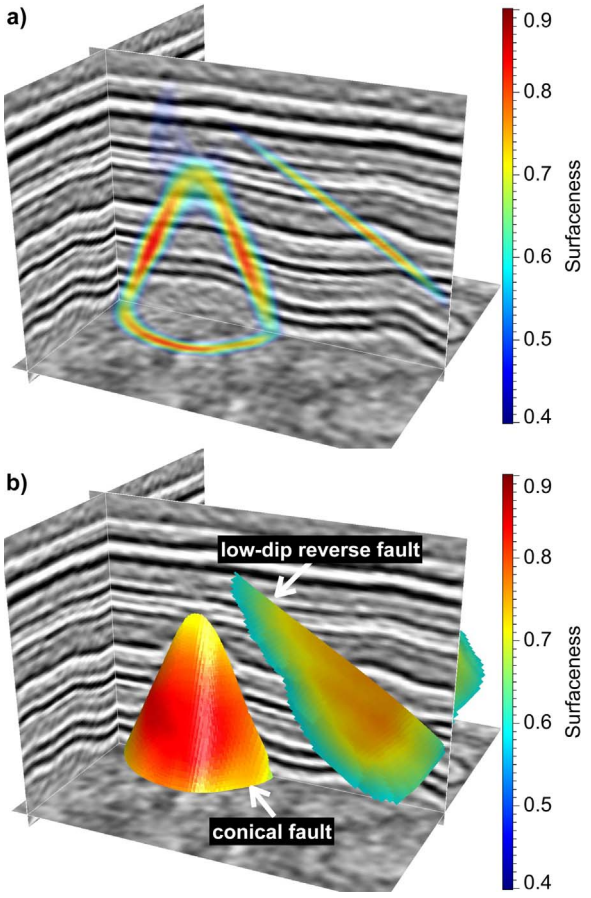


**Fig. 9.** Fault samples are first computed from the matched filtering method (Algorithm 1) and then used in the tensor voting processing to compute a fault surfaceness attribute volume (a) overlaid with the seismic volume. A conical fault surface and a low-dip reverse fault surface (b) are finally extracted from the fault surfaceness volume (a).

intersection shown in Fig. 4(c). This gap is generated by the missing fault samples at the intersection. Fault samples are also missing at some other locations where holes are observed on the constructed faults A, B, and C. The holes or incomplete fault surfaces may cause problems for estimating fault slips that correlate seismic reflections on opposite sides of a fault surface (Wu et al., 2016). In the next section, we will discuss a more robust method to construct complete fault surfaces without holes from sparse fault samples.

## 3. Fault surface construction

It may be difficult to directly link the fault samples to construct fault surfaces in complicated cases with missing fault samples and noisy samples unrelated to faults. In these cases, we suggest to use the *tensor-voting* method (Guy and Medioni, 1993; Tang, 2000; Moreno et al., 2011), proposed in computer graphics, to infer fault surfaces that accurately fit the positions and orientations of the samples and reasonably fill gaps.

### 3.1. Tensor voting

Construction of fault surfaces from oriented fault samples (Fig. 4(a)) is similar to the problem of surface reconstruction from scattered points, which is well studied in computer graphics. Numerous methods (Kazhdan et al., 2006; Lipman et al., 2007; Guennebaud and Gross, 2007; Kazhdan and Hoppe, 2013; Berger et al., 2014) have been proposed to compute reasonable surfaces that fit the given points. We choose the tensor-voting method to construct fault surfaces because it can deal with intersecting surfaces.

3D tensor voting can infer surfaces and curves (including surface intersections) from oriented or unoriented points through *stick*, *plate*, and *ball* voting (Tang, 2000; Moreno et al., 2011). In this paper, we use the stick-tensor voting to infer fault surfaces and surface intersections from fault samples which are oriented by fault strikes and dips. In the tensor-voting method, we first represent each oriented fault sample $\mathbf{q}$ as a stick tensor $\mathbf{S_q}$ weighted by its fault attribute value $h_\mathbf{q}$:

$$\mathbf{S_q} = h_\mathbf{q}\mathbf{u_q}\mathbf{u_q}^\top, \tag{5}$$

where the unit vector $\mathbf{u_q} = [u_1\ u_2\ u_3]^\top$ is the fault normal vector computed from the strike and dip angles of the fault sample $\mathbf{q}$. We then apply the stick tensor-voting process to propagate the tensor of a fault sample to its nearby samples by assuming the tensors of neighboring samples vary smoothly. By doing this, we are able to enhance consistent tensors corresponding to fault samples that are aligned in local planes while suppressing noisy tensors corresponding to noisy samples.

Fig. 5 shows an example of the stick tensor-voting process, in which the *voter* sample $\mathbf{q}$ propagates a voting tensor $\mathbf{V}(\mathbf{r}, \mathbf{S_q})$ to a nearby *receiver* sample $\mathbf{p}$. This voting tensor $\mathbf{V}(\mathbf{r}, \mathbf{S_q})$ is inferred by tracking the change of the normal on a smooth curve connecting the voter and receiver. Although the connection can be any smooth curve, a circular arc, as denoted by $s$ in Fig. 5, is commonly used to infer a voting tensor. Using a circular arc, we compute a voting tensor $\mathbf{V}(\mathbf{r}, \mathbf{S_q})$ that is aligned with the radius vector defined by the receiver $\mathbf{p}$ and the center of the circular arc $s$, as shown in Fig. 5. This voting tensor is often weighted by a function that decays with the length and curvature of the circular arc $s$.

From the geometry shown in Fig. 5, it is not difficult to prove that

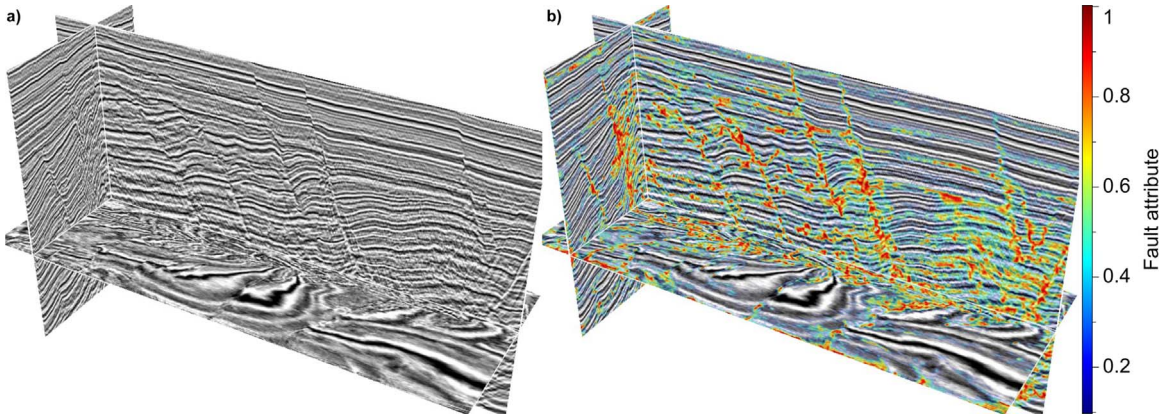


**Fig. 10.** A 3D seismic volume (a) displayed with a fault attribute volume (b), which is computed from a seismic semblance volume.

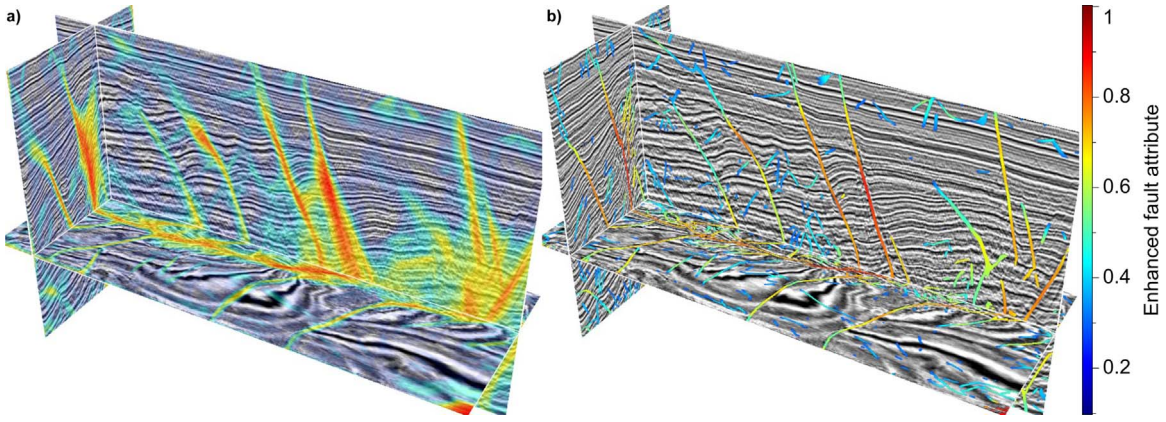


**Fig. 11.** The matched filtering method is applied to the fault attribute volume in Fig. 10(b) to compute an enhanced attribute volume (a), which is thinned in (b).

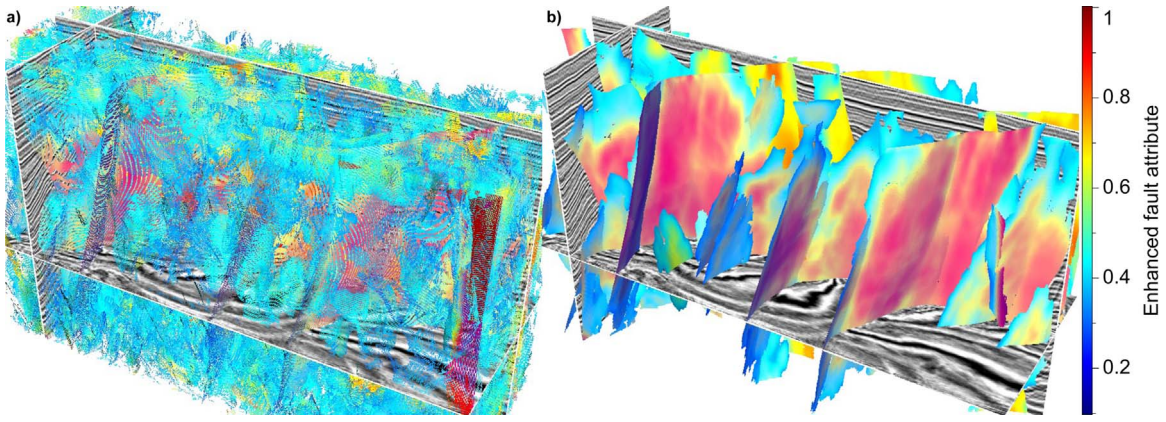


**Fig. 12.** Fault samples (a) are directly linked to form fault surfaces (b).

the voting tensor $\mathbf{V}(\mathbf{r}, \mathbf{S_q})$ is rotated by $2\alpha$ comparing to the known tensor $\mathbf{S_q}$. Therefore, we are able to compute the voting tensor $\mathbf{V}(\mathbf{r}, \mathbf{S_q})$ at a receiver $\mathbf{p}$ by simply rotating and scaling the known tensor $\mathbf{S_q}$ at the corresponding voter $\mathbf{q}$:

$$\mathbf{V}(\mathbf{r}, \mathbf{S_q}) = w(\mathbf{r}, \mathbf{S_q})\mathbf{R}_{2\alpha}\mathbf{S_q}\mathbf{R}_{2\alpha}^{\top}, \tag{6}$$

where $\alpha$ is the angle shown in Fig. 5, and $\mathbf{R}_{2\alpha}$ represents a rotation matrix.

The weighting function in Eq. (6) can be defined as a Gaussian function with length and curvature of the circular arc $s$ (Tang, 2000; Mordohai and Medioni, 2006):

$$w(\mathbf{r}, \mathbf{S_q}) = \begin{cases} e^{-\frac{s^2+c\kappa^2}{\sigma^2}}, & \text{if } \alpha \le \pi/4, \\ 0, & \text{otherwise} \end{cases} \tag{7}$$

where $c$ and $\sigma$ are parameters can be defined by users. The arc length $s$ and its curvature $\kappa$ are given by

$$s = \frac{\| \mathbf{r} \| \alpha}{\sin\alpha} \text{ and } \kappa = \frac{2\sin\alpha}{\| \mathbf{r} \|}, \tag{8}$$

respectively.

To improve computational efficiency, we use a similar but simpler weighting function suggested by Franken et al. (2006):

$$w(\mathbf{r}, \mathbf{S_q}) = \begin{cases} e^{-\frac{\|\mathbf{r}\|^2}{\sigma^2}}\cos\alpha^{2n}, & \text{if } \alpha \le \pi/4. \\ 0, & \text{otherwise} \end{cases} \tag{9}$$

In this weighting function, we choose a Gaussian that decays with the distance between the voter and receiver. We use $\cos\alpha^{2n}$, a function

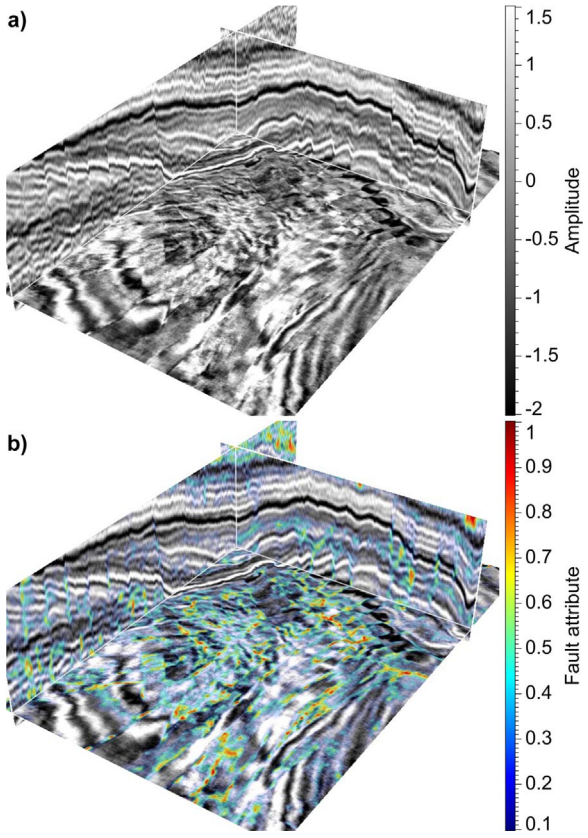


**Fig. 13.** A 3D seismic volume (a) is displayed with a fault attribute volume (b), which is computed from a seismic semblance volume.

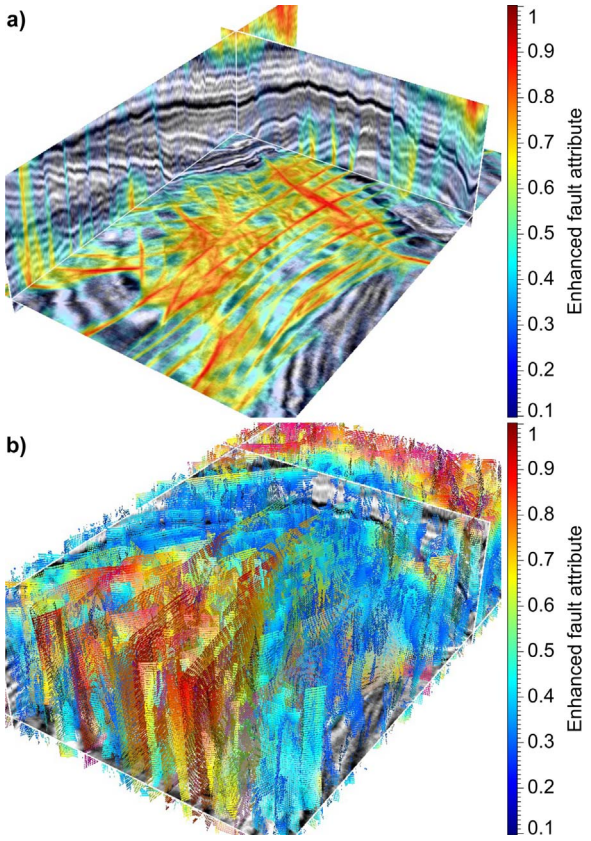


**Fig. 14.** An enhanced fault attribute volume (a) and fault strike and dip volumes (not shown) are first computed from the input attribute volume (Fig. 13(b)) by using the matched filtering method. Fault samples (b) are colored by enhanced fault attribute and oriented by fault strikes and dips.

decays with $\alpha$, to penalize high-curvature arcs connecting the voters and receivers. $n$ is a constant number ($n > 1$), and bigger $n$ results in faster decay with $\alpha$.

Using the voting function defined in Eq. (6), we compute an output tensor $\mathbf{U}(\mathbf{x})$ at each sample $\mathbf{x}$ by accumulating voting tensors from all fault samples in its neighborhood $\Omega(\mathbf{x})$:

$$\mathbf{U}(\mathbf{x}) = \sum_{\substack{\mathbf{q}\in\Omega(\mathbf{x}) \\ \mathbf{r}=\mathbf{x}-\mathbf{q}}} \mathbf{V}(\mathbf{r}, \mathbf{S}_\mathbf{q}). \tag{10}$$

The neighborhood $\Omega(\mathbf{x})$ of a sample $\mathbf{x}$ is defined by a 3D box window centered at $\mathbf{x}$, and the angle $\alpha$ (Fig. 5) should be smaller than $\frac{\pi}{4}$ because the weighting function $w(\mathbf{r}, \mathbf{S}_\mathbf{q}) = 0$ for $\alpha \geq \frac{\pi}{4}$ as defined in Eq. (9). In our examples, fault samples are sparsely scattered in a 3D volume, we use the KD-tree method (Friedman et al., 1977) to efficiently search for nearby fault samples in the neighborhood of a sample $\mathbf{x}$.

### 3.2. Surfaceness and fault intersection

After computing a voted tensor $\mathbf{U}(\mathbf{x})$ for each sample $\mathbf{x}$, we are able to estimate degrees of *surfaceness* and *curveness* at the sample $\mathbf{x}$ by computing saliency measurements from the tensor. High surfaceness values indicate fault positions, while high curveness values indicate fault intersections.

The tensor $\mathbf{U}$, computed from the tensor voting (Eq. (10)), is a 3×3 symmetric, non-negative definite matrix with eigen-decomposition:

$$\mathbf{U} = \lambda_1\mathbf{e}_1\mathbf{e}_1^\top + \lambda_2\mathbf{e}_2\mathbf{e}_2^\top + \lambda_3\mathbf{e}_3\mathbf{e}_3^\top, \tag{11}$$

where $\mathbf{e}_1$, $\mathbf{e}_2$, and $\mathbf{e}_3$ are eigenvectors and $\lambda_1$, $\lambda_2$, and $\lambda_3$ are the corresponding eigenvalues ($\lambda_1 \geq \lambda_2 \geq \lambda_3$). This eigen-decomposition can be rewritten as

$$\mathbf{U}(\mathbf{x}) = (\lambda_1 - \lambda_2)\mathbf{e}_1\mathbf{e}_1^\top + (\lambda_2 - \lambda_3)(\mathbf{e}_1\mathbf{e}_1^\top + \mathbf{e}_2\mathbf{e}_2^\top) + \lambda_3(\mathbf{e}_1\mathbf{e}_1^\top + \mathbf{e}_2\mathbf{e}_2^\top + \mathbf{e}_3\mathbf{e}_3^\top).$$

As discussed in Tang (2000), the first term means that the fault samples near the sample $\mathbf{x}$ infer a single surface passing through $\mathbf{x}$. The scalar $\lambda_1 - \lambda_2$ indicates certainty of such a single surface and therefore is defined as surfaceness. The vector $\mathbf{e}_1$ in the first term indicates orientation (normal direction) of the single surface. The second term describes that nearby fault samples infer two surfaces intersecting at the sample $\mathbf{x}$. The corresponding scalar $\lambda_2 - \lambda_3$ indicates certainty of surface intersection, and therefore is defined as curveness. The third term describes that nearby fault samples infer multiple surfaces intersecting at the sample. The corresponding scalar $\lambda_3$ is defined as ballness because it indicates certainty of a case where surfaces with all orientations are equally probable at the sample.

To illustrate the tensor-voting method for fault surface construction, we apply the method to the fault samples on the incomplete fault surfaces with holes (Fig. 4(b)) to reconstruct more complete fault surfaces. As the computational cost of tensor-voting processing in Eq. (10) is dependent of the number of fault samples, we randomly choose only twenty five percent of the fault samples on the fault surfaces (Fig. 4(b)). From these sparsely chosen fault samples (Fig. 6(a)), we then construct a tensor $\mathbf{S}_\mathbf{q}$ for each oriented sample using Eq. (5). Next, we apply the tensor-voting processing to the constructed tensors and obtain a voted tensor field $\mathbf{U}(\mathbf{x})$ using Eq. (10). We finally apply eigen-decomposition to the voted tensor field and obtain a surfaceness volume $\lambda_1 - \lambda_2$ (Fig. 6(b)) and a intersection volume $\lambda_2 - \lambda_3$ (Fig. 6(c)). Relatively high values in the surfaceness volume indicate locations of the fault surfaces, while those high values in the intersection volume indicate the locations of the surface intersection.

We observe that the fault features in this surfaceness volume

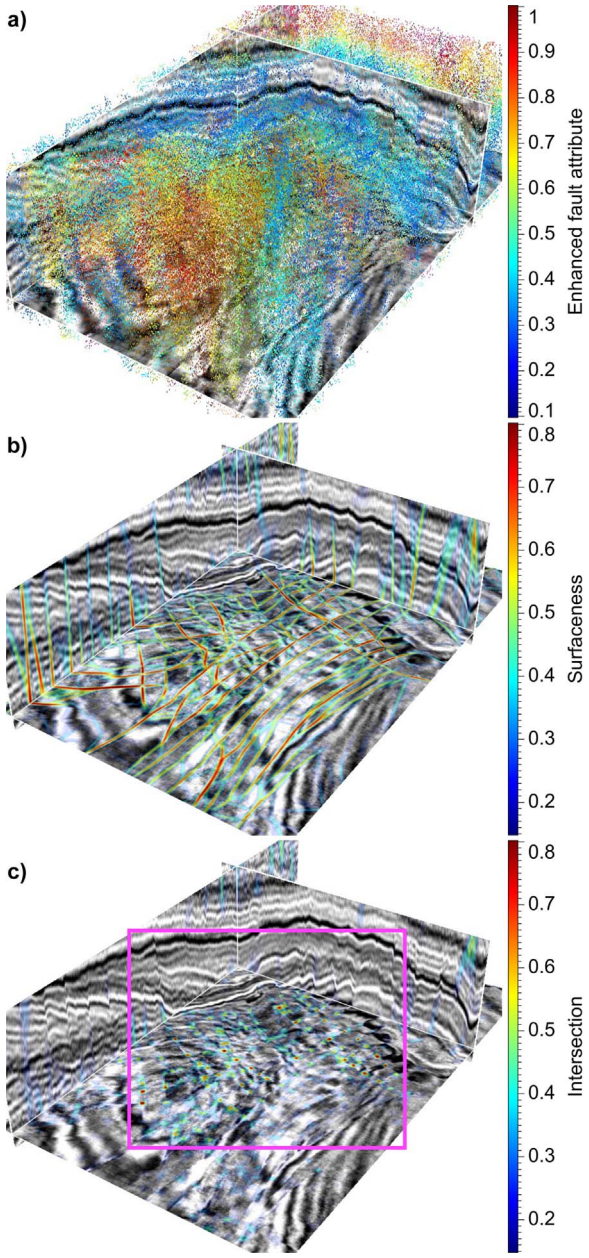


**Fig. 15.** Twenty five percent of fault samples (a) are randomly chosen from Fig. 14(b). These fault samples (a) are used to compute another volumes of surfaceness (b) and fault intersection (c).

(Fig. 6(b)) are much cleaner and more consistent than those in the original fault attribute volume (Fig. 1(b)), the fault likelihood volume (Fig. 1(c)), and the enhanced fault attribute volume (Fig. 2(a)). From this surfaceness volume (Fig. 6(b)), we are able to extract more complete fault surfaces without holes as shown in Fig. 7(a). The intersection volume is also important to construct complete intersecting fault surfaces (Fig. 7(b)) without gaps at the intersection because it tells us the locations (areas with high values in Fig. 7(c)) where we should attempt to construct multiple surfaces.

The 3D synthetic example in Fig. 7 shows that our methods are applicable to extract planar and high-dip fault surfaces. To demonstrate that our methods also work well to extract curved and low-dip fault surfaces, we created another 3D synthetic seismic volume (Fig. 8a) with a low-dip reverse fault and a cone-shaped normal fault as denoted by the white dashed curves in Fig. 8(b). A conical fault appears a specially curved cone-shaped surface with the full range of fault strike angles from 0° to 360°. Such specially shaped fault surfaces

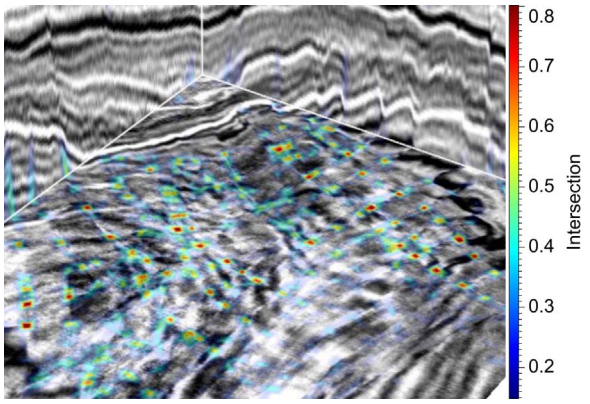


**Fig. 16.** A close view of the fault intersection volume in the magenta box in Fig. 15(c).

are demonstrated to be apparent in real 3D seismic volumes as discussed by Hale and Groshong (2014). Fig. 8(b) shows a fault attribute volume (1-semblance) computed from the synthetic seismic amplitude volume (Fig. 8a). Relatively high values in this fault attribute volume highlight some positions of the faults. These fault features (with relatively high fault attribute values), however, are discontinuous and widely separated or interrupted. Fault surfaces are difficult to be extracted directly from such discontinuous fault features.

With this fault attribute volume (Fig. 8b), we first apply the matched filtering method (Algorithm 1) to compute three volumes of enhanced fault attribute, fault strikes and dips. From these three computed volumes, we then construct oriented fault samples, which are further used to compute a fault surfaceness volume shown in Fig. 9a. The fault features in this surfaceness volume (Fig. 8a) are much more obvious and continuous than those in the fault attribute volume in Fig. 8(b). From such a surfaceness volume, we are able to extract the low-dip reverse fault surface and the curved conical fault surface shown in Fig. 9(b).

## 4. Application

We have used a 3D synthetic example (Fig. 1(a)) to illustrate the whole processing for enhancing fault attributes, estimating fault orientations, and extracting fault surfaces. To further demonstrate the whole processing, we apply the methods discussed above to two 3D examples with and without intersecting faults.

The first 3D seismic volume shown in Fig. 10(a) is from offshore Indonesia. From this seismic volume, we first compute a structure-oriented semblance volume $p(\mathbf{x})$ and obtain the fault attribute volume shown in Fig. 10(b) by $1 - p(\mathbf{x})$. Relatively high values in this fault attribute volume indicate positions of faults. However, some of these high values, especially those horizontally aligned, are caused by noise or other reflector discontinuities unrelated to faults. In addition, the fault features are widely separated and discontinuous.

We then apply the fault-oriented smoothing method to compute an enhanced fault attribute volume (Fig. 11(a)) and at the same time obtaining fault strike and dip volumes (not shown). In this enhanced volume (Fig. 11(a)), horizontally aligned noisy features are suppressed comparing to those in the original fault attribute volume (Fig. 10(b)). The fault features in this enhanced volume (Fig. 11(a)) are cleaner and more continuous than those in Fig. 10(b). The thinned fault attribute volume in Fig. 11(b) is obtained by keeping only the values on the ridges of the enhanced fault attribute volume in Fig. 11(a). We also compute the corresponding thinned fault strike and dip volumes which are not shown in this paper.

From the three thinned volumes of enhanced fault attribute, fault strike, and fault dip, we then construct the fault samples shown in Fig. 12(a). These fault samples are oriented by fault strikes and dips, and are colored by the enhanced fault attribute values. Most samples

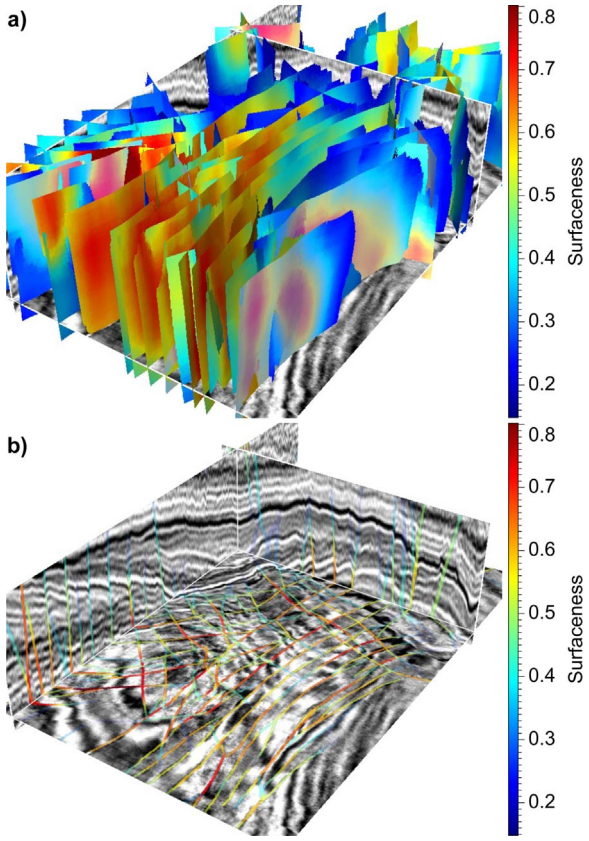


**Fig. 17.** Fault surfaces (a) are constructed using the surfaceness (Fig. 15(b)) and fault intersection (Fig. 15(c)) volumes. These surfaces, colored by surfaceness, are displayed as a volume of surfaceness overlaid with the seismic volume in (b).

with relatively high values (colored by red) are aligned approximate planes, consistent with locally planar fault surfaces. Noisy fault samples, often with low fault attribute values, are also observed in Fig. 12(a). However, these samples are misaligned and often cannot be linked together to form locally planer fault surfaces with significant sizes.

Our final step for this example is to directly link nearby fault samples with consistent fault strikes and dips to construct fault surfaces in Fig. 12(b). We display only the surfaces with significant sizes in Fig. 12(b) while discard those with small numbers of linked fault samples. As the fault geometry is simple in this example, the fault surfaces, extracted by directly linking nearby fault samples, are continuous and complete as shown in Fig. 12(b). Therefore, the tensor-voting processing is not necessary in this example to construct fault surfaces, which requires extra time to compute a voted tensor field.

Compared to the first example, the fault geometry in the second example (Fig. 13(a)) is more complicated because a lot of intersecting faults are apparent in this example. Similar to the processing applied to the first example, we first compute a structure-oriented semblance volume and a fault attribute volume (1-semblance) as shown in Fig. 13(b). Fault surfaces are difficult to extract from this fault attribute volume because the fault features are inconsistent and disconnected as shown in Fig. 13(b).

We then apply the fault-oriented smoothing method to compute an enhanced fault attribute volume (Fig. 14(a)) and corresponding fault strike and dip volumes (not shown). The fault features in this enhanced volume are more continuous and consistent than those in the original fault attribute volume (Fig. 13(b)). However, it is still difficult to construct complete fault surfaces from this enhanced fault volume because the corresponding fault samples (Fig. 14(b)) are noisy and fault samples may be missing at the fault intersections.

We then apply the tensor-voting processing to the oriented fault samples to better construct fault surfaces. To improve computational efficiency, we randomly choose only twenty five percent of the fault samples (Fig. 14(b)). In the tensor-voting processing, tensors are constructed for all the sparse fault samples (Fig. 15(a)) using the strikes and dips of the samples. These tensors are then used to compute a voted tensor $\mathbf{U}(\mathbf{x})$ for each sample $\mathbf{x}$. Eigen-decomposition is then applied to the tensor field $\mathbf{U}(\mathbf{x})$ to compute a surfaceness volume (Fig. 15(b)) and an intersection volume (Fig. 15(c)). The fault features (colored by red) in this surfaceness volume are much cleaner and more consistent than those in the enhanced fault volume. A lot of red squares are observed on the horizontal slice of the intersection volume (Fig. 15(c)) and the close view of the volume in Fig. 16. These red squares indicate locations of fault intersections.

Using the surfaceness and intersection volumes, we finally construct complete fault surfaces without holes as shown in Fig. 17(a). Many of the constructed fault surfaces intersect with each other as shown on the horizontal slice in Fig. 17(b), where the fault surfaces are displayed as a surfaceness volume overlaid with the seismic volume.

## 5. Conclusion

We first discussed a matched filtering method to enhance an input fault attribute volume while at the same time computing volumes of fault strikes and dips. We then discussed methods to construct fault surfaces from the three volumes of enhanced fault attribute, fault strikes, and fault dips.

In the matched filtering method, any fault attribute or multiple attributes can be used to compute the three fault volumes, from which we can construct oriented fault samples on the ridges of the enhanced fault attribute volume. For most cases with simple fault geometry (without intersecting faults), fault surfaces can be constructed by directly linking the nearby fault samples with consistent fault strikes and dips. For more complicated cases with multiple intersecting fault surfaces and noisy fault samples, we suggest to use the tensor-voting method to more accurately construct complete fault surfaces without holes.

The computational cost of the matched filtering method is dependent on the scanning ranges of the fault strikes and dips. In our definitions, the strike range is from 0° to 360° and the dip range is theoretically from 0° to 90°. In most cases, we use a smaller range of dips because faults are often more vertical than horizontal. If priori knowledge of the strike ranges is available, we should apply the fault-oriented scanning and smoothing only in the known strike range to reduce the computational cost. In constructing fault surfaces using tensor voting, the cost is dependent on the number of fault samples obtained from the fault-oriented smoothing. These fault samples are often densely aligned on potential fault planes. We suggest to randomly and sparsely choose only a subset of the samples for the tensor-voting processing. In most of our tests, twenty five percent of randomly selected fault samples are enough for the tensor voting to reasonably infer fault surfaces.

## Acknowledgments

The real 3D seismic volume in Fig. 10(a) is graciously provided by Clyde through Paradigm. The real 3D seismic volume shown in Fig. 13(a) is graciously provided by the Dutch Government through TNO and dGB Earth Sciences.

## References

Admasu, F., Back, S., Toennies, K., 2006. Autotracking of faults on 3D seismic data. Geophysics 71 (6), A49–A53.

Aqrawi, A.A., Boe, T.H., 2011. Improved fault segmentation using a dip guided and modified 3D Sobel filter In: Proceedings of the 81st Annual International Meeting, SEG, Expanded Abstracts, pp. 999–1003.

Bakker, P., 2002, Image structure analysis for seismic interpretation: Bakker, P., 2002, Image structure analysis for seismic interpretation: Ph.D. Thesis, Delft University of Technology.

Berger, M., Tagliasacchi, A., Seversky, L., Alliez, P., Levine, J., Sharf, A., Silva, C., 2014. State of the art in surface reconstruction from point clouds: EUROGRAPHICS star reports, pp. 161–185.
Cohen, I., Coult, N., Vassiliou, A.A., 2006. Detection and extraction of fault surfaces in 3D seismic data. Geophysics 71 (4), P21–P27.
Fehmers, G.C., Höcker, C.F., 2003. Fast structural interpretation with structure-oriented filtering. Geophysics 68 (4), 1286–1293.
Fomel, S., 2002. Applications of plane-wave destruction filters. Geophysics 67 (6), 1946–1960.
Franken, E., van Almsick, M., Rongen, P., Florack, L., ter Haar Romeny, B., 2006. An efficient method for tensor voting using steerable filters. In: Proceedings of the 9th European Conference on Computer Vision - Volume Part IV, Springer-Verlag, pp. 228–240.
Friedman, J.H., Bentley, J.L., Finkel, R.A., 1977. An algorithm for finding best matches in logarithmic expected time: ACM Transactions on Mathematical Software.
Gersztenkorn, A., Marfurt, K.J., 1999. Eigenstructure-based coherence computations as an aid to 3-D structural and stratigraphic mapping. Geophysics 64 (5), 1468–1479.
Gibson, D., Spann, M., Turner, J., Wright, T., 2005. Fault surface detection in 3-D seismic data: geoscience and Remote sensing. IEEE Trans. 43, 2094–2102.
Guennebaud, G., Gross, M., 2007. Algebraic point set surfaces: Presented at the ACM SIGGRAPH 2007 Papers, ACM.
Guy, G., Medioni, G., 1993. Inferring global perceptual contours from local features. In: Proceedings of IEEE Computer Society Conference on Computer Vision and Pattern Recognition, Proceedings CVPR '93., 1993, pp. 786–787.
Hale, D., 2009. Structure-oriented smoothing and semblance: CWP Report 635.
Hale, D., 2013. Methods to compute fault images, extract fault surfaces, and estimate fault throws from 3D seismic images. Geophysics 78 (2), O33–O43.
Hale, D., Groshong, R.H., 2014. Conical faults apparent in a 3d seismic image. Interpretation 2 (1), T1–T11.
Kadlec, B.J., Dorn, G.A., Tufo, H.M., Yuen, D.A., 2008. Interactive 3-D computation of fault surfaces using level sets. Vis. Geosci. 13, 133–138.
Kazhdan, M., Bolitho, M., Hoppe, H., 2006. Poisson surface reconstruction. In: Proceedings of the Fourth Eurographics Symposium on Geometry Processing.
Kazhdan, M., Hoppe, H., 2013. Screened Poisson surface reconstruction. ACM Trans. Graph. (TOG) 32, 29.
Lipman, Y., Cohen-Or, D., Levin, D., Tal-Ezer, H., 2007. Parameterization-free projection for geometry reconstruction. ACM Trans. Graph. (TOG) 26, 22.
Marfurt, K.J., 2006. Robust estimates of 3D reflector dip and azimuth. Geophysics 71 (4), P29–P40.
Marfurt, K.J., Kirlin, R.L., Farmer, S.L., Bahorich, M.S., 1998. 3-D seismic attributes using a semblance-based coherency algorithm. Geophysics 63 (4), 1150–1165.
Marfurt, K.J., Sudhaker, V., Gersztenkorn, A., Crawford, K.D., Nissen, S.E., 1999. Coherency calculations in the presence of structural dip. Geophysics 64 (1), 104–111.
Mordohai, P., Medioni, G., 2006. Tensor voting: a perceptual organization approach to computer vision and machine learning. Synth. Lect. Image Video, Multimed. Process. 2, 1–136.
Moreno, R., Garcia, M., Puig, D., Pizarro, L., Burgeth, B., Weickert, J., 2011. On improving the efficiency of tensor voting. IEEE Trans. Pattern Anal. Mach. Intell. 33, 2215–2228.
Neff, D.B., Grismore, J.R., Lucas, W.A., 2000. Automated seismic fault detection and picking. (US Patent 6,018,498).
Pedersen, S.I., Randen, T., Sonneland, L., Steen, Ø. 2002, Automatic fault extraction using artificial ants In: Proceedings of the 72nd Annual International Meeting, SEG, Expanded Abstracts, pp. 512–515.
Pedersen, S.I., Skov, T., Hetlelid, A., Fayemendy, P., Randen, T., Sønneland, L., 2003. New paradigm of fault interpretation In: Proceedings of the 73rd Annual International Meeting, SEG, Expanded Abstracts, 350–353.
Randen, T., Pedersen, S.I., Sønneland, L., et al., 2001. Automatic extraction of fault surfaces from three-dimensional seismic data In: Proceedings of the 81st Annual International Meeting, SEG, Expanded Abstracts, pp. 551–554.
Schultz, T., Theisel, H., Seidel, H.P., 2010. Crease surfaces: from theory to extraction and application to diffusion tensor MRI. IEEE Trans. Vis. Comput. Graph. 16, 109–119.
Tang, C.-K., 2000. Tensor voting in computer vision, visualization, and higher dimensional inferences: Ph.D. Thesis, University of Southern California, University of Southern California.
Van Bemmel, P.P., Pepper, R.E., 2000. Seismic signal processing method and apparatus for generating a cube of variance values. (US Patent 6,151,555).
Van Vliet, L.J., Verbeek, P.W., 1995. Estimators for orientation and anisotropy in digitized images In: Proceedings of the First Annual Conference of the Advanced School for Computing and Imaging ASCI'95, Heijen (The Nether- lands), pp. 442–450.
Wang, Z., AlRegib, G., 2014. Fault detection in seismic datasets using hough transform: 2014 IEEE International Conference on Acoustics, Speech and Signal Processing (ICASSP), pp. 2372–2376.
Wang, Z., AlRegib, G. et al., 2014. Automatic fault surface detection by using 3D hough transform In: Proceedings of the 84th Annual International Meeting, SEG, Expanded Abstracts, pp. 1439–1444.
Wu, X., 2016. Methods to compute salt likelihoods and extract salt boundaries from 3D525 seismic images. Geophysics 81 (6), IM119–IM126.
Wu, X., 2017. Directional structure-tensor based coherence to detect seismic faults and channels. Geophysics 82 (2), A13–A17.
Wu, X., Hale, D., 2016. 3D seismic image processing for faults. Geophysics 81 (2), IM1–IM11.
Wu, X., Luo, S., Hale, D., 2016. Moving faults while unfaulting 3D seismic images. Geophysics 81 (2), IM25–IM33.